

Tension Estimation and Localization for a Tethered Micro Aerial Robot

Ricardo Martins and Meysam Basiri

Abstract

This work focuses on the study of tethered flights of a micro quadcopter, with the aim of supplying continuous power to a small-sized aerial robot. Multiple features for facilitating the interaction between a tethered micro quadcopter and a ground base are described in this paper. Firstly, a tether model based on the catenary curve is presented that describes a quadcopter tethered to a point in space. Furthermore, a method capable of estimating the tension applied to the quadcopter, based only on the inertial information from the IMU sensors and the motor thrusts, is presented. Finally, a novel method for localizing the quadcopter by exploiting the tension imposed by the tether and the shape of the tether is described. The proposed methods are evaluated both in simulation and in real world prototype.

1 Introduction

Micro aerial robots are known by their versatility and ability to get information from higher altitudes allowing them to have many important applications [1, 2, 3, 4]. However, such robots have a low payload capacity and due to the small on-board battery short flight times are reached. In some applications where the robot is only required to operate inside a limited air space, such as to inspect a solar panel installation [3], an industrial structure [5] or a vessel [6] or to operate inside a house [7], continuous power can be supplied through a tether that is attached to a ground station allowing beyond battery missions [8]. The ground station can also be mobile, such as a mobile service robot [9] or an unmanned ground vehicle [10], to further extend the operation area of the tethered aerial robot and to perform missions cooperatively with the aerial/ground multi robot system [11]. The integration of a tethered micro aerial robot can also enhance the capabilities of mobile ground robots by providing an aerial perspective of the surrounding environment, facilitating tasks such as path planning and obstacle avoidance [12, 13].

To implement a tethered solution, the cable characteristics for the tether must be carefully considered taking into account the resistance and the varying power drop across the cable [14, 15]. Although it is possible

to only power an aerial robot through a tether, however, a small on-board battery could also be used to allow robustness against power blackouts or damages to the tether [16].

Ground robots, with their ability to carry large payloads, including batteries, sensors, and computers, offer a unique opportunity for collaboration with aerial robots [10]. By combining their strengths, the two types of robots can undertake tasks that would otherwise be impossible individually. Aerial robots, for example, can provide valuable aerial sensing and enhance the ground robots' localization capabilities [17]. Conversely, ground robots can serve as mobile charging stations or power sources, supplying energy to their aerial counterparts via an attached tether [17, 18, 19].

Despite the benefits mentioned above, there are multiple challenges that must be considered to facilitate autonomous operation of tethered aerial robots. The constraints in the motion of the robot imposed by the tether and the varying tension that the tether applies to the robot must be considered by the flight controller. For this purpose, it is important to have an accurate estimation of this varying tension.

In this paper a method to estimate the tension on a tethered aerial robot is described that is only based on the IMU sensor readings. As the IMU measurements have high noise levels which prevents them from being used directly for accurate tension estimations, a filtering approach is used to assist with the estimation. Furthermore, we show that the robot position estimation can be improved by exploiting the properties of the tether and using the tension applied to the UAV. The tension on the end-points of the tether is related to its shape, which means that the relation between the tether model and the tension applied to the quadcopter can be expressed mathematically.

2 Proposed Methodologies

2.1 Characterization of the shape of the tether

2.1.1 Catenary Curve

In case of a non-rigid tether connecting the quadcopter to a ground-base, the shape of the tether approximately outlines a catenary curve. The catenary model consists of a hanging cable, with no stiffness, sagging under its own weight and supported only by its ends (see figure 1). The point (x_1, y_1) corresponds

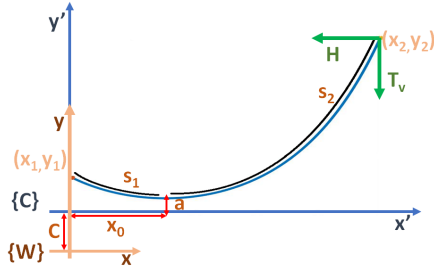


Figure 1: Catenary curve and related parameters; world $\{W\}$ and catenary $\{C\}$ frames.

to the origin and the point (x_2, y_2) to the position of the quadcopter. The shape of the catenary can be defined according to a mathematical model, in which expression 1 presents the **equation of the catenary**.

$$y = a \cdot \cosh\left(\frac{x - x_0}{a}\right) + C \quad (1)$$

Parameter $\langle x_0 \rangle$ is the abscissa of the lowest point. Parameter $\langle a \rangle$ corresponds to the y coordinate of the lowest point of the curve ($x = x_0$) regarding the catenary frame $\{C\}$, and it must always be positive.¹ Parameter $\langle C \rangle$ is an offset between the world frame $\{W\}$ and the catenary frame $\{C\}$, which depends on the tether's parameter $\langle a \rangle$ and the y coordinate of the lowest point regarding the world frame (y_0).

$$C = y_0 - a \quad (2)$$

Expressions 3 and 4 introduce the tether parameters $\langle s_1 \rangle$ and $\langle s_2 \rangle$, which represent the arc-length from the tether lowest point to the origin and to the UAV, respectively.

$$s_1 = a \cdot \sinh\left(\frac{|x_1 - x_0|}{a}\right) \quad (3)$$

$$s_2 = a \cdot \sinh\left(\frac{|x_2 - x_0|}{a}\right) \quad (4)$$

Equations 5 and 6 respectively present the horizontal and vertical tension on the end-points of the catenary curve. Both the horizontal and vertical tension depend on the tether's parameters - $\langle a \rangle$ or $\langle s \rangle$ - and on the weight of the tether, where ω is the weight per length unit [20].

$$H = \omega \cdot a \quad (5)$$

$$T_V = \omega \cdot s \quad (6)$$

The absolute value of the tension results from the euclidean norm of the horizontal and vertical tensions.

$$|T| = \sqrt{T_V^2 + H^2} \quad (7)$$

The quadcopter flying in an R^3 space allows to define the horizontal tension (H) in terms of a component along the x direction and another along the y direction, as shown in figure 2. The previous circumstance

¹A negative value of parameter $\langle a \rangle$ would only have a physical meaning if the shape of the catenary was concave instead of convex.

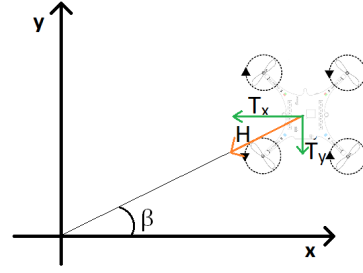


Figure 2: Horizontal tension decomposition.

relates the tension along the x and y direction according equation 8 and 9, respectively.

$$Tx = \cos(\beta) \cdot |H| \quad (8)$$

$$Ty = \sin(\beta) \cdot |H| \quad (9)$$

The parameters of the catenary cannot be mathematically computed by only knowing the coordinates of the two tether end-points. Thus, these parameters - $\langle a \rangle$, $\langle x_0 \rangle$, $\langle C \rangle$, $\langle s_1 \rangle$, and $\langle s_2 \rangle$ - are obtained gathering additional information from knowing the full length of the tether.

This assumption leads to a possible and determined system of equations 10-14, which can be numerical solved generating the curve parameters.

$$y_1 = a \cdot \cosh\left(\frac{x_1 - x_0}{a}\right) + C \quad (10)$$

$$y_2 = a \cdot \cosh\left(\frac{x_2 - x_0}{a}\right) + C \quad (11)$$

$$s_{total} = s_2 + s_1 \quad (12)$$

$$s_1 = a \cdot \sinh\left(\frac{|x_1 - x_0|}{a}\right) \quad (13)$$

$$s_2 = a \cdot \sinh\left(\frac{|x_2 - x_0|}{a}\right) \quad (14)$$

Subtracting equation 10 from equation 11, and making use of the hyperbolic cosine properties, it follows:

$$\Delta Y = 2a \cdot \sinh\left(\frac{\Delta x}{a}\right) \cdot \sinh\left(\frac{x_{average} - x_0}{a}\right), \quad (15)$$

where $\Delta x = \frac{x_2 - x_1}{2}$, $x_{average} = \frac{x_2 + x_1}{2}$ and $\Delta y = y_2 - y_1$. The expression of the length of the tether $\langle s_{total} \rangle$ is re-written by replacing equation 13 and 14 into expression 12, and using the hyperbolic sine properties.

$$s_{total} = 2a \cdot \sinh\left(\frac{\Delta x}{a}\right) \cdot \cosh\left(\frac{x_{average} - x_0}{a}\right), \quad (16)$$

Equation 17 presents a useful relation between $\langle x_0 \rangle$ and $\langle a \rangle$, which results from the division of ΔY by $\langle s_{total} \rangle$.

$$x_0 = x_{average} - a \cdot \tanh^{-1}\left(\frac{\Delta Y}{s_{total}}\right) \quad (17)$$

The insertion of equation 17 in equation 15 allows to obtain equation 18, and using the Newton-Raphson method on this last produces the value of parameter

$\langle a \rangle$. However, when $\Delta Y = 0$ it is not possible to compute parameter $\langle a \rangle$ since equation 18 does not depend on $\langle a \rangle$ to be valid. Nevertheless, from the knowledge that $\Delta Y = 0$ it comes that x_0 is known and corresponds to $x_{average}$, which means that equation 16 can compute the parameter $\langle a \rangle$. An alternative approach is to force the value of ΔY to be not null by adding a small offset.

$$\Delta Y - 2.a.\sinh\left(\frac{\Delta x}{a}\right).\sinh\left(\tanh^{-1}\left(\frac{\Delta Y}{s_{total}}\right)\right) = 0 \quad (18)$$

The expansion of the Taylor series derives the initial estimation of parameter $\langle a \rangle$.

$$\sinh(x) = \frac{e^x - e^{-x}}{2} = \sum_{n=0}^{\infty} \frac{x^{2n+1}}{(2n+1)!} = x + \frac{x^3}{3!} + \frac{x^5}{5!} + \dots \quad (19)$$

By applying this approximation to expression 18, one can re-write this last equation as a result of a 5th order approximation for the hyperbolic sine, according to equation 20.

$$\left(\frac{\Delta Y}{2.\sinh(\tanh^{-1}(\frac{\Delta Y}{s_{tot}}))} - \Delta x \right) a^4 - \frac{\Delta x^3}{3!} a^2 - \frac{\Delta x^5}{5!} = 0 \quad (20)$$

The assumption that $\alpha = a^2$ reduces equation 20 to the 2nd order. Furthermore, the quadratic formula presented in equation 21 produces the solution for this 2nd order expression

$$x^2 = \frac{-b \pm \sqrt{b^2 - 4.a.c}}{2.a}, \quad (21)$$

where

$$a = \frac{\Delta Y}{2.\sinh(\tanh^{-1}(\frac{\Delta Y}{s_{total}}))} - \Delta x, b = \frac{-\Delta x^3}{3!}, c = \frac{-\Delta x^5}{5!}. \quad (22)$$

Reverting the variable substitution produces the desired value for $\langle a \rangle$, according to equation 20.

$$a = \sqrt{\langle \alpha \rangle}, \quad (23)$$

Since equation 20 is a 4th order equation it produces 4 roots - in the relevant domain, two of them are complex roots and two of them real roots, one positive and other negative. Only the positive real root has a physical meaning and so it is the only one to be taken into account.

The replacement of $\langle x_0 \rangle$ and $\langle a \rangle$ into equation 10 or into equation 11 allows to compute the $\langle C \rangle$ parameter.

2.1.2 Validation of the catenary model

The malleability of the tether is one of the most important feature to ensure that the tether outlines a catenary curve. The validation of the catenary model was done by overlaying the real silicon tether with the theoretical model of the catenary curve, as shown in figure 3.

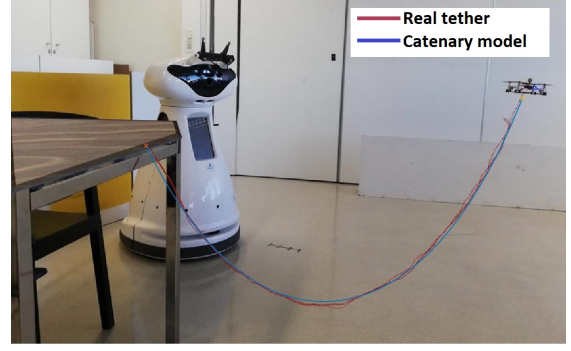


Figure 3: Catenary model validation

2.2 Tension Estimation

The tension estimate applied to the quadcopter is computed using the quadcopter's thrust and the inertial information from its IMU sensors. However, these sensor readings present a high level of noise, which means that it is impossible to determine the tension applied to the quadcopter with the desired accuracy. To filter the undesired noise, and assuming that the noise is white Gaussian, a Kalman filter was implemented.

Equations 24 and 25 describe a linear system, in which w_k and v_k are the process and the observation noise, respectively; x_k is the system's state vector; y_k is the observation vector of the system's states; u_k is the system's input.

$$x_k = Ax_{k-1} + Bu_k + w_k \quad (24)$$

$$y_k = Cx_k + D + v_k \quad (25)$$

The Kalman filter starts by propagating the process model, where \hat{x}_k^- is the state estimate.

$$\hat{x}_k^- = A\hat{x}_{k-1} + Bu_k \quad (26)$$

Afterwards, it uses the information from the sensor measurements to improve the estimate obtained from the model propagation. The final state estimate is given by:

$$\hat{x}_k = \hat{x}_k^- + K_k(y_k - C\hat{x}_k^-) \quad (27)$$

The variable K_k is the Kalman gain, which adjusts the relation between the process and observation estimates.

The tension that is applied to the quadcopter may be applied through human interaction, which implies infinite possibilities for the way that the wire is pulled. The implemented solution considers a model where the tension remains the same, which can be extended to situations where the wire is not abruptly pulled and do not have considerable oscillations.

The state estimate (\hat{x}_k) is a \mathbb{R}^3 vector, including the tension along x , y and z directions, and y_k is the observation vector, which includes the tension measurements.

$$\hat{x}_k = \begin{bmatrix} Tx_k \\ Ty_k \\ Tz_k \end{bmatrix} \quad y_k = \begin{bmatrix} Tx_k^{obs} \\ Ty_k^{obs} \\ Tz_k^{obs} \end{bmatrix} \quad (28)$$

$$A = C = [I]^{3 \times 3} \quad B = D = [\emptyset]^{3 \times 1}$$

The tension measurements T^{obs} are obtained through equation 29, where \vec{a} corresponds to the acceleration vector, \vec{g} to the gravity vector, $R(\eta)$ to the rotation matrix between the world and the quadcopter frames (see figure 4), and F_p to the total thrust of the quadcopter. The superscript obs refers to the on-board sensor reading of the quadcopter.

$$T^{obs} = m(\vec{a}^{obs} + \vec{g}) - R(\eta)^{obs} F_p^{obs} + F_{ext} \quad (29)$$

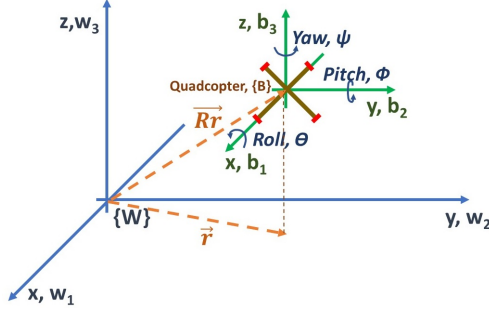


Figure 4: World frame W , body frame B , radial vector \vec{R}_r , and its horizontal projection \vec{r}

2.3 Position Estimation

This section² uses the relation between the tension that the catenary model exerts to the quadcopter and its parameters to compute the position estimate of the quadcopter. The curve parameters $\langle a \rangle$ and $\langle s_2 \rangle$ are computed according to equations 30 and 31, where the horizontal H and vertical T_v tensions are obtained using the methods presented in section 2.2.

$$a = \frac{H}{\omega} \quad (30)$$

$$s_2 = \frac{T_v}{\omega} \quad (31)$$

The curve parameters $\langle a \rangle$ and $\langle s_2 \rangle$ are then used to compute the spatial coordinates of the end of the tether attached to the UAV, along with the knowledge of the tether's full length $\langle s_{tot} \rangle$.

$$s_{tot} = s_2 + s_1 \quad (32)$$

This way, replacing x_0 by r_0 and x_1 by r_i in equation 13, and using the relation presented in equation 32, one can derive equation 33.

$$r_0 = r_i + a \cdot \sinh^{-1}\left(\frac{s_{tot} - s_2}{a}\right) \quad (33)$$

Furthermore, replacing x_0 by r_0 and x_2 by r in equation 14, the radial distance r comes as:

$$r = r_0 + a \cdot \sinh^{-1}\left(\frac{s_2}{a}\right) \quad (34)$$

²In section 2.1 the catenary model was evaluated for a \mathbb{R}^2 space. In this section, the quadcopter is moving in a \mathbb{R}^3 , and so the y and x coordinates in section 2.1 are replaced by z and r coordinates, where $r = \sqrt{x^2 + y^2}$ (see figure 4)

At last, equation 35 uses the catenary's expression and computes the quadcopter's altitude,

$$z = a \cdot \cosh\left(\frac{r - r_0}{a}\right) + C \quad (35)$$

where equation 36 computes parameter $\langle C \rangle$.

$$C = z_i - a \cdot \cosh\left(\frac{r_i - r_0}{a}\right) \quad (36)$$

If the horizontal tension H is null, equations 34 and 35 have a mathematical indetermination of type $0 \times \infty$. The limits of those equations are presented in equations 37 and 38.

$$\lim_{a \rightarrow 0} z = \lim_{a \rightarrow 0} a \cdot \cosh\left(\frac{r}{a}\right) + C = z_i + |s_2| - |s_1| \quad (37)$$

$$\lim_{a \rightarrow 0} r = \lim_{a \rightarrow 0} a \cdot \sinh^{-1}\left(\frac{s_1}{a}\right) + a \cdot \sinh^{-1}\left(\frac{s_2}{a}\right) = 0 \quad (38)$$

3 Experimental results

3.1 Estimation of the vertical tension

The validation of the vertical tension estimate is done by performing a vertical tethered takeoff, which represents the simplest experiment to compute its ground-truth value Tv_{gt} . This last one is calculated through



Figure 5: Illustration of the vertical tension estimation experiment

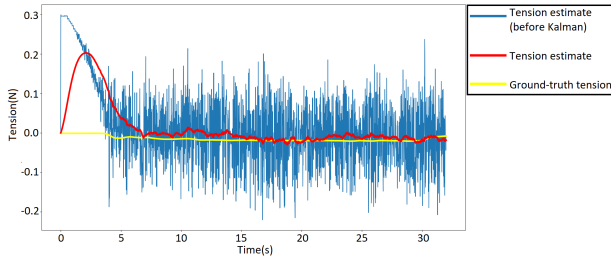
the height of the quadcopter z , and the weight per length unit of the the tether ω .

$$Tv_{gt} = \omega \cdot z \quad (39)$$

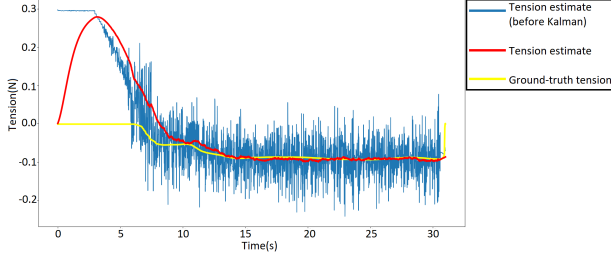
Figure 6 illustrates the vertical tension estimates. The tension estimation procedure does not take into account the force that the ground exerts on the quadcopter while the propellers are not spinning, i.e., that are not counter balancing its weight. Thus, in the initial instants, the vertical tension estimate does not correspond to its ground-truth values and the 0,3N value approximately corresponds to the weight of the quadcopter.

3.2 Estimation of the horizontal tension

To validate the horizontal tension estimate, its ground-truth value is computed using a small mass (coin) attached to a wire. Figure 7 illustrates the scheme of the test-bench used to compute the ground-truth values for the horizontal tension. Equation 40 computes



(a) Hovering at a height of 0,3m.



(b) Hovering at a height of 1,3m.

Figure 6: Ground-truth values and estimates of the vertical tension applied to the UAV.

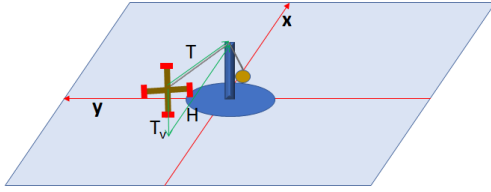


Figure 7: Test-bench for computing the horizontal tension.

the ground-truth value of the horizontal tension, in which T corresponds to the weight of the mass and γ is computed according to equation 41 - z_q and z_a are the height of the quadcopter and the height of the vertical arm, respectively, and r_q is the quadcopter's radial coordinate, assuming the inertial frame presented in figure 7.

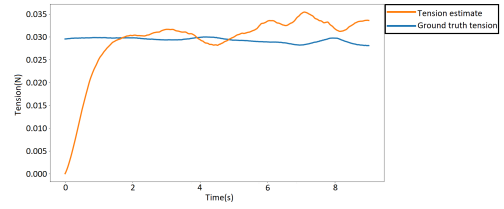
$$H = \cos(\gamma) \cdot T \quad (40)$$

$$\gamma = \tan^{-1}\left(\frac{z_q - z_a}{r_q}\right) \quad (41)$$

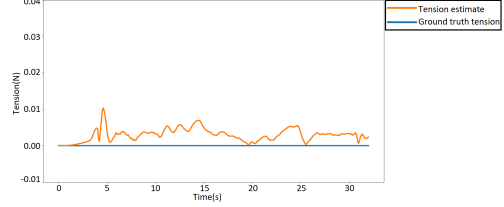
Figure 8(a) displays the tension estimate and the ground-truth value for an attached mass of 4,1g, and figure 8(b) shows the result for a tethered vertical takeoff, where the tether direction is mainly vertical. As figure 8(b) displays, the horizontal tension estimate is nearly null - less than 0.01N.

3.3 Tension following

The tension applied to the quadcopter is estimated in real-time, according to section 2.2. The goal position of the quadcopter changes if the estimated tension is greater than a pre-defined threshold. When this occurs, the goal position of the quadcopter is successively updated to its current position, making it to follow the pull's direction. When the tension applied



(a) Hovering flight at position $x = -0.3$, $y = z = 0$.



(b) Hovering flight at $x = y = 0$ and $z = 0.4$.

Figure 8: Ground-truth values and estimates of the horizontal tension applied to the UAV.

to the quadcopter is no longer greater than the pre-defined threshold, the goal position stops being updated and the quadcopter remains hovering at its last position.

To observe the behaviour of the *tension following* feature a few videos were taken ³, where figures 9 and 10 correspond to screenshots of those videos. More-



Figure 9: Screenshots of the quadcopter following the tension's direction.

over, the implementation of the *tension following* feature can also be used for the landing process. Given that, after the first tug, a flag is activated indicating that the *tension following* feature is on. Thus, if the quadcopter flies under a certain height, the motors are turned off. Without using an external motion system, the same principle can be applied using a sensor distance, which deactivates the motors if the distance to the landing platform is smaller than a threshold. Figure 10 illustrates the mentioned landing process.



Figure 10: Screenshots of the landing of the quadcopter using the *tension following* feature.

3.4 Position estimation

To avoid the modeling of the tether's oscillations, the results presented throughout this section concern hovering flights. Additionally, the angle β , which relates the radial distance with the x and y coordinates, was

³The full videos are presented on Youtube [here](#).

also a source of inaccuracy. It was initially assumed that the β angle was known and was computed using the Mocap system. In practice, the angle β could be computed using a visual or mechanical system on the ground controller that could indicate the direction of the tether. Figure 11 presents a pair of experiments in which the height corresponds to 1m and the radial distances are similar between them. In a second set of

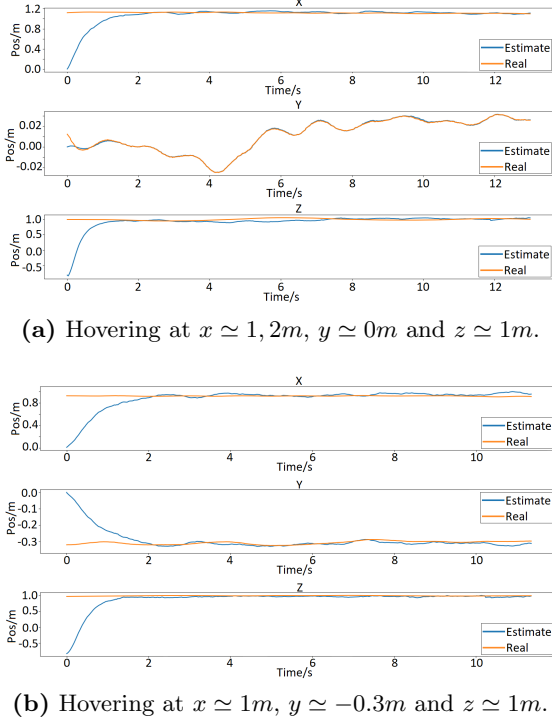


Figure 11: Hovering at same height z and similar radial distance (x, y) for small angle β (< 20).

experiments (figure 12) the radial distances are also similar between them but the estimation of the quadcopter's height is evaluated for two different heights - 0.5m and 1.2m. A third set of experiments (figure 13) is performed with a bigger range for the value of the y coordinate. In the initial instants the Kalman filter assumes that the tensions T_x and T_y are null, which means that the length $\langle s_2 \rangle$ and the tether parameter $\langle a \rangle$ also start to be zero (see equations 42 and 43).

$$s_2 = \frac{T_v}{\omega} \quad (42)$$

$$a = \frac{H}{\omega} \quad (43)$$

According to the expression deduced in equation 38, the initial estimated position of the radial coordinate is null, implying that x and y coordinates are also null. On the one hand, equation 37 allows to infer that the initial estimate regarding the altitude corresponds to $z_i - |s_1|$, since s_2 is zero. On the other hand, the tether's total length is given by equation 32, which means that $s_1 = s_{tot}$ for a null length s_2 . Equation 44 presents the initial estimate of the altitude over this set of experiments.

$$z = z_i - |s_1| = 0.754 - 1.6 = -0.846 \quad (44)$$

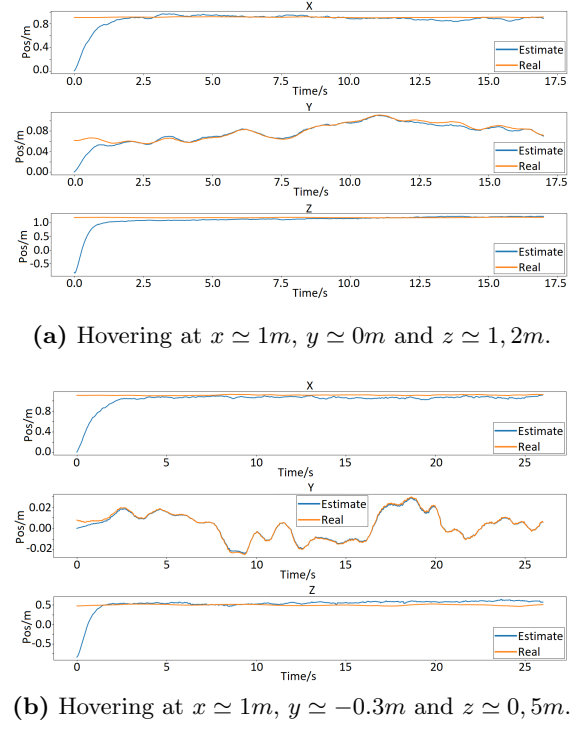


Figure 12: Hovering at different heights z and similar radial distance (x, y) for small angle β (< 10).

4 Conclusions

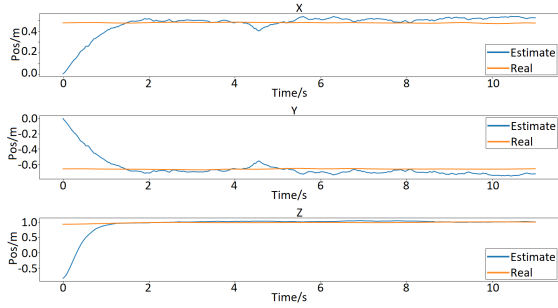
This work presented a method to estimate the tension applied to a quadrotor by using measurements from the IMU sensors. Due to the high level of noise, two Kalman based filtering processes were introduced. Furthermore, the tension estimate was used to present alternative ways of controlling the quadcopter, and to improve the position estimate of a tethered quadcopter.

The first flight control strategy used the tension estimate to update the quadcopter's position. Nevertheless, the position of the quadcopter must be known through an external motion system. Aiming to develop a control strategy that does not need to know the position of the UAV, a novel methodology that uses the tether's shape and the tension estimate was introduced.

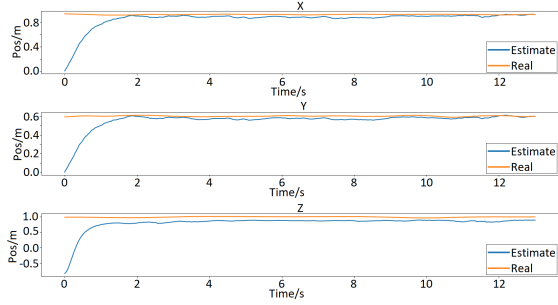
Moreover, this study presented a method to estimate the position of the quadcopter based on the tension that the tether applies to the UAV and its shape.

References

- [1] Meysam Basiri, Felix Schill, Pedro U.Lima, and Dario Floreano. Localization of emergency acoustic sources by micro aerial vehicles. *Journal of Field Robotics*, 35(2):187–201, 2018.
- [2] Miguel Pimentel and Meysam Basiri. A bimodal rolling-flying robot for micro level inspection of flat and inclined surfaces. *IEEE Robotics and Automation Letters*, 7(2):5135–5142, 2022.



(a) Hovering at $x \simeq 0,5m$, $y \simeq -0.6m$ and $z \simeq 1m$.



(b) Hovering at $x \simeq 0,9m$, $y \simeq 0.6m$ and $z \simeq 1m$.

Figure 13: Hovering at same height z and different radial distance (x, y) for non-small angle $\beta (> 30)$.

- [3] Yahya Zefri, Achraf Elkettani, Imane Sebari, and Sara Ait Lamallam. Inspection of Photovoltaic Installations by Thermo-visual UAV Imagery Application Case: Morocco. In *2017 International Renewable and Sustainable Energy Conference (IRSEC)*, pages 1–6, Tangier, December 2017. IEEE.
- [4] Hakan Kayan, Raheleh Eslampanah, Faezeh Yeganli, and Murat Askar. Heat leakage detection and surveillance using aerial thermography drone. In *2018 26th Signal Processing and Communications Applications Conference (SIU)*, pages 1–4, Izmir, Turkey, May 2018. IEEE.
- [5] Michael Burri, Janosch Nikolic, Christoph Hurzeler, Gilles Caprari, and Roland Siegwart. Aerial service robots for visual inspection of thermal power plant boiler systems. In *2012 2nd International Conference on Applied Robotics for the Power Industry (CARPI)*, pages 70–75. IEEE, September 2012.
- [6] Alberto Ortiz, Francisco Bonnin-Pascual, and Emilio Garcia-Fidalgo. Vessel Inspection: A Micro-Aerial Vehicle-based Approach. *Journal of Intelligent & Robotic Systems*, 76(1):151–167, September 2014.
- [7] Rômulo T. Rodrigues, Meysam Basiri, A. Pedro Aguiar, and Pedro Miraldo. Feature based potential field for low-level active visual navigation. In Anibal Ollero, Alberto Sanfeliu, Luis Montano, Nuno Lau, and Carlos Cardeira, editors, *ROBOT 2017: Third Iberian Robotics Conference*, pages 791–800, Cham, 2018. Springer International Publishing.
- [8] Brendan Galea and Paul G Kry. Tethered flight control of a small quadrotor robot for stippling. In *2017 IEEE/RSJ International Conference on Intelligent Robots and Systems (IROS)*, pages 1713–1718. IEEE, 2017.
- [9] Rodrigo Ventura, Meysam Basiri, André Mateus, Joao Garcia, Pedro Miraldo, Pedro Santos, and Pedro U Lima. A domestic assistive robot developed through robot competitions. In *IJCAI 2016 Workshop on Autonomous Mobile Service Robots*, 2016.
- [10] Meysam Basiri, João Gonçalves, José Rosa, Rui Bettencourt, Alberto Vale, and Pedro Lima. A multipurpose mobile manipulator for autonomous firefighting and construction of outdoor structures. *Field Robot*, 1:102–126, 2021.
- [11] Andrea Borgese, Dario C. Guastella, Giuseppe Sutera, and Giovanni Muscato. Tether-based localization for cooperative ground and aerial vehicles. *IEEE Robotics and Automation Letters*, 7(3):8162–8169, 2022.
- [12] Mohammad Amin Basiri, Shirin Chehelgami, Erfan Ashtari, Mehdi Tale Masouleh, and Ahmad Kalhor. Synergy of deep learning and artificial potential field methods for robot path planning in the presence of static and dynamic obstacles. In *2022 30th International Conference on Electrical Engineering (ICEE)*, pages 456–462, 2022.
- [13] S. Martínez-Rozas, D. Alejo, F. Caballero, and L. Merino. Optimization-based trajectory planning for tethered aerial robots. In *2021 IEEE International Conference on Robotics and Automation (ICRA)*, pages 362–368, 2021.
- [14] Seiga Kiribayashi, Jun Ashizawa, and Keiji Nagatani. Modeling and design of tether powered multicopter. In *2015 IEEE International Symposium on Safety, Security, and Rescue Robotics (SSRR)*, pages 1–7. IEEE, 2015.
- [15] Peter Savnik. *Tether Control for Unmanned Aerial Vehicle - Creating a Platform for Tether Control of UAV*. PhD thesis, 01 2015.
- [16] Wasantha Samarathunga, Guangwei Wang, and Shiqin Wang. Auxiliary power unit evaluation for tethered uav. *International Journal of New Technology and Research*, 2(7).
- [17] Jesús Morales, Isabel Castelo, Rodrigo Serra, Pedro U. Lima, and Meysam Basiri. Vision-based autonomous following of a moving platform and landing for an unmanned aerial vehicle. *Sensors*, 23(2), 2023.

- [18] Seiga Kiribayashi, Kaede Yakushigawa, and Keiji Nagatani. Design and development of tether-powered multirotor micro unmanned aerial vehicle system for remote-controlled construction machine. In *Field and Service Robotics*, pages 637–648. Springer, 2018.
- [19] Robert Severinghaus and John Kaniarz. Quadrotor for increased situational awareness for ground vehicles. Technical report, Army Tank Automotive Research Development and Engineering center warren MIARMY, 2015.
- [20] E.Russel Johnston Ferdinand P.Beer. *Mecânica Vetorial para Engenheiros, Estática, Volume I*. McGraw-Hill, 1980.